Revision 1

Word Count: 6386

Atomistic insight into the ferroelastic post-stishovite transition by high-pressure single-crystal X-ray diffraction refinements

YANYAO ZHANG[1,*], STELLA CHARITON[2], JIAMING HE[3], SUYU FU[1,5], FANG XU[4], VITALI B. PRAKAPENKA[2], JUNG-FU LIN[1,*]

[1]Department of Geological Sciences, Jackson School of Geosciences, The University of Texas at Austin, Austin, TX 78712, USA

[2]Center for Advanced Radiation Sources, The University of Chicago, IL 60637, USA

[3]Materials Science and Engineering Program, Mechanical Engineering, The University of Texas at Austin, Austin, Texas 78712, USA

[4]Department of Earth Sciences, University College London, Gower Street, London WC1E 6BT, UK

[5]Present address: School of Earth and Space Exploration, Arizona State University, Tempe, AZ 85287, USA

*****Corresponding authors: Yanyao Zhang (yanyaozhang@utexas.edu), Jung-Fu Lin (afu@jsg.utexas.edu)

Running title: atomistic insight of post-stishovite transition

ABSTRACT

The post-stishovite transition is a classic pseudo-proper typed ferroelastic transition with a symmetry-breaking spontaneous strain. This transition has been studied using high-pressure spontaneous strains, optic modes, and elastic moduli (C_{ij}) based on the Landau modeling, but its atomistic information and structural distortion remain poorly understood. Here we have conducted synchrotron single-crystal X-ray diffraction measurements on stishovite crystals up to 75.3 GPa in a diamond-anvil cell. Analysis of data reveals atomic positions, bond lengths, bond angles, and variations of SiO_6 octahedra across the transition at high pressure. Our results show that the oxygen coordinates split at approximately 51.4 GPa where the apical and equatorial Si-O bond lengths cross over, the SiO_6 octahedral distortion vanishes, and the SiO_6 octahedra start to rotate about the *c* axis. Moreover, distortion mode analysis shows that an in-plane stretching distortion (GM_1^+ mode) occurs in the stishovite structure at high pressure while a rotational distortion (GM_2^+ mode) becomes dominant in the post-stishovite structure. These results are used to correlate with elastic moduli and Landau parameters (symmetry-breaking strain e_1 - e_2 and order parameter Q) to provide atomistic insight into the ferroelastic transition. When the bond lengths of two Si-O bonds are equal due to the contribution from the GM_1^+ stretching mode, C_{11} converges with C_{12} and the shear wave $V_{S1[110]}$ propagating along $[1\bar{1}0]$ and polarizing along [110] vanishes. Values of e_1 - e_2 and Q are proportional to the SiO_6 rotation angle from the occurrence of the GM_1^+ rotational mode in the post-stishovite structure. Our results on the pseudo-proper type transition are also compared with that for the proper-type in albite and improper-type in $CaSiO_3$ perovskite. The symmetry-breaking strain in all these types of transitions arises as the primary effect from the structural angle (such as SiO_6 rotation or lattice constant angle) and its relevant distortion mode in the low-symmetry ferroelastic phase.

Keywords: single-crystal X-ray diffraction, stishovite, post-stishovite, ferroelastic transition, structural angle, distortion mode, Landau model, spontaneous strain

INTRODUCTION

Ferroelastic phase transitions occur in silicate minerals in the Earth's interior because of temperature and pressure perturbations. These transitions in crystals involve a change in point group with a symmetry-breaking strain (Aizu, 1969; Aizu, 1970). According to the Landau theory, there are different types of the ferroelastic transitions, including proper, pseudo-proper, and improper types, which have different transition mechanisms (Carpenter and Salje, 1998; Wadhawan, 1982). The proper-type transition is driven by the symmetry-breaking spontaneous strain, whereas the pseudo-proper- and improper-type transitions are driven by other physical properties that are linearly and nonlinearly coupled to the symmetry-breaking strain, respectively (Carpenter et al., 1998; Wadhawan, 1982). These types of the ferroelastic phase transitions are also well known to be associated with elastic and optic mode anomalies including sound wave velocity softening, which could occur in some naturally abundant minerals under high pressure-temperature (*P*-*T*) conditions in the Earth's crust and mantle (Carpenter, 2006; Salje, 1990; Salje, 1992). Knowing their transition mechanisms and elastic properties in relevant *P*-*T* conditions can help us understand geophysics and geodynamics of the Earth's interior. For example, the proper-type ferroelastic transition in feldspar, comprising of approximately 41 wt% of the continental crust (Rudnick et al., 2003), has been linked to seismic low-velocity anomaly in the crust (Brown et al., 2006; Liu et al., 2018; Waeselmann et al., 2016; Zhang and Klemperer, 2005; Zhao et al., 2001). The stishovite and $CaSiO_3$ perovskite (CaPv) are abundant phases in the subducted mid-ocean ridge basalt (MORB) in the lower mantle (Ishii et al., 2019). Their transition mechanisms

This is the peer-reviewed, final accepted version for American Mineralogist, published by the Mineralogical Society of America.
The published version is subject to change. Cite as Authors (Year) Title. American Mineralogist, in press.
DOI: https://doi.org/10.2138/am-2022-8458. http://www.minsocam.org/

and elastic anomalies have been used to explain seismic heterogeneities, to infer the presence of the subducting slabs, and to constrain mantle convection at depths (Helffrich, 2006; Kaneshima, 2016; Niu et al., 2003; Sun et al., 2020; Thomson et al., 2019; Wang et al., 2020). As a prototype of six-fold coordinated silicates, the ferroelastic transition in stishovite is particularly important not only to aid our understanding in physical properties of subducting slabs in the mantle (Lakshtanov et al., 2007; Tsuchiya, 2011; Yang and Wu, 2014; Zhang et al., 2021), but also to shed light on similar phase transitions in other rock-forming silicate and oxide minerals at depths.

The ferroelastic transition across the stishovite to post-stishovite phases at 50-55 GPa has been relatively well investigated using multiple experimental data sets including optical Raman modes, lattice constants from powder X-ray diffraction, and elastic moduli (C_{ij}) derived from sound velocities (Andrault et al., 2003; Buchen et al., 2018; Kingma et al., 1995; Lakshtanov et al., 2007; Zhang et al., 2021). These data are further complemented by Landau theory modeling (Carpenter et al., 2000; Hemley et al., 2000) and ab initio calculations (Karki et al., 1997a; Karki et al., 1997b; Yang and Wu, 2014). Importantly, experimental optic modes and lattice parameters across the transition have been used in the pseudo-proper type Landau modeling to show that the transition is driven by the soft B_{1g} mode and accompanied by a symmetry-breaking spontaneous strain and a significant shear softening (Andrault et al., 2003; Carpenter et al., 2000; Hemley et al., 2000; Kingma et al., 1995). A recent experimental study on C_{ij} of stishovite across the post-stishovite transition has further showed that C_{11} converges with C_{12} at the transition pressure, where the shear wave $V_{S1[110]}$ propagating along $[1\bar{1}0]$ and polarizing along [110] vanishes (Zhang et al., 2021). These results reveal macroscopic physical phenomena that need to be integrated with microscopic atomic displacements in order to have a complete understanding of

the transition and its physical properties. Along this line, crystal structural parameters, such as oxygen positions, bond lengths, and bond angles, are key to microscopically quantifying elastic anomalies and some Landau parameters such as the symmetry-breaking spontaneous strain. A previous powder X-ray diffraction (PXRD) study has refined crystal structures of stishovite and post-stishovite phases at high pressure using the Rietveld structural analysis method (Andrault et al., 1998). However, the refined structural parameters showed considerable scattering at high pressure due to difficulties in solving crystal structures from the powder diffraction data (Harris et al., 2001). On the other hand, high-resolution single-crystal X-ray diffraction (SCXRD) studies on the stishovite are limited to 30 GPa, far below the transition pressure (Hill et al., 1983; Ross et al., 1990; Sinclair and Ringwood, 1978; Sugiyama et al., 1987; Yamanaka et al., 2002). This limitation was mainly due to the technical difficulty in conducting high-resolution SCXRD experiments at high pressure using a laboratory X-ray source. Recent advance in synchrotron X-ray diffraction technique now enables reliable crystal structure refinements to better understand the transition and elastic anomalies from the microscopic atomic perspective (Boffa Ballaran et al., 2013; Chariton et al., 2020; Clegg, 2019; Dera, 2010)

In this study, we performed synchrotron SCXRD experiments on stishovite crystals up to 75.3 GPa in a diamond anvil cell (DAC) with large X-ray opening equipped with Boehler-Almax anvils and seats. The crystal structure of the stishovite or post-stishovite phase has been solved and refined at each experimental pressure. Refined structural parameters show that the oxygen coordinates split at the transition pressure of ~51.4 GPa where the bond lengths of apical and equatorial Si-O bonds are equal. This atomic information is further used to evaluate deformation and rotation of the SiO_6 octahedron across the transition. Two symmetry modes, GM_1^+ and GM_2^+, are analyzed to reveal crystal structure distortion at high pressure. Our results show that a

rotational mode with GM_2^+ symmetry occurs at the transition pressure where the SiO_6 octahedron starts to rotate about the *c* axis. Furthermore, we correlate the microscopic bond length difference of two Si-O bonds with the macroscopic elastic properties in the literature, such as C_{11}, C_{12}, and $V_{S1[110]}$ (Zhang et al., 2021). The symmetry-breaking spontaneous strain e_1 - e_2 and order parameter Q in a pseudo-proper type Landau model are quantified using the SiO_6 rotation angle Φ that comes from the GM_2^+ mode. Together with early studies on other types of the ferroelastic transitions (Kroll et al., 1980; Zhao et al., 1993a; Zhao et al., 1993b), we therefore conclude that the symmetry-breaking strain changes linearly with a given structural angle in all types of ferroelastic transition.

EXPERIMENTAL METHODS AND DATA ANALYSIS

Stishovite single crystals were synthesized using a 1000-ton Kawai-type multi-anvil apparatus at the Institute for Planetary Materials, Okayama University (run# 1K1642). The synthesis and characterization of the crystals has been reported elsewhere (Xu et al., 2017; Zhang et al., 2021). Briefly, reagent-grade silicic acid of 99.9% purity (SiO_2 with 13 wt% H_2O) was used as the starting sample which was loaded into a platinum capsule. The sample assemblage was compressed to 12 GPa and then heated to 1873 K. The temperature of the assemblage was slowly cooled down to 1473 K with a rate of 100 K/hour (4 hours in total) before quenched to ambient temperature and then decompressed to ambient pressure. Stishovite crystals recovered from the sample capsule are transparent and free of twinning domains and inclusions under optical and petrographic microscopes (Zhang et al., 2021). Electron microprobe analyses of a number of selected crystals show a chemical formula of SiO_2 without any other detectable elements. Analysis of unpolarized Fourier-transform infrared spectroscopic spectra shows ~19 ppm wt.

water content in the selected crystals (Xu et al., 2017; Zhang et al., 2021). The amount of water in the Al-free stishovite crystals is consistent with previous reports (Litasov et al., 2007; Pawley et al., 1993).

Three stishovite crystals were loaded into a short-symmetric DAC with a pair of Boehler-Almax designed diamond anvils mounted onto WC seats with a large aperture of ~80º (4θ). This allowed us to obtain reflections at a wide two theta range (2θ, Figure S1). The culet size of the diamond anvils is 200 μm in diameter. A rhenium gasket with an initial thickness of 260 μm was pre-indented to ~24 μm thick and subsequently a hole of 120 μm diameter was drilled in the center of the pre-indented area and used as the sample chamber. To obtain more reflections from stishovite, we selected three stishovite crystals with (2.4, 4.7, 1.7), (-0.8, 0.3, 1.6), and (0.8, 2.2, -0.9) orientations, respectively, which were determined by SCXRD measurements. The crystals were double-side polished down to approximately 7 μm thick using 3M diamond films. They were then cut into ~10-20 μm big platelets before being loaded into the sample chamber (Figure 1). Au powder (Goodfellow; 99.95% purity) was pressed into 2 μm thick, cut into ~5 μm wide disks, and placed close to the center of the sample chamber as the pressure calibrant (Fei et al., 2007). The three stishovite platelets were loaded at an equal distance to the Au calibrant to minimize possible pressure gradient across the crystals in the chamber (Figure 1c). Neon gas was loaded into the sample chamber as the pressure medium using a gas loading system at the Mineral Physics Laboratory of the University of Texas at Austin.

High-pressure SCXRD experiments were conducted up to 75.3 GPa at room temperature at 13ID-D beamline of the GSECARS, Advanced Photon Source, Argonne National Laboratory (Figures 1a and 1b). An incident X-ray beam of 0.2952 Å wavelength (42 keV energy) was focused down to a beam size of ~3×3 μm^2 at the sample position. Approximately 10% intensity

of the incident X-ray was used for the measurements to avoid peak saturations. The sample stage was rotated over ±31º about the vertical axis of the DAC during data collections. The XRD patterns were collected using a CdTe Pilatus 1M detector with 1 or 2 s exposure time at every 0.5º step of the rotation. A membrane was used to increase and control pressure in the sample chamber. After each pressure increase, we monitored the pressure of the sample chamber until it was stabilized before SCXRD measurements were conducted. Pressure uncertainties were evaluated from analysis of XRD spectra of Au collected right before and after each set of SCXRD measurements (Fei et al., 2007). Additionally, SCXRD measurements at ambient conditions were conducted in the Department of Chemistry at the University of Texas at Austin. A stishovite crystal with dimensions of approximately 0.94 × 0.44 × 0.17 mm was selected for the experiment. A SuperNova dual source diffractometer equipped with a Mo Kα radiation source (λ = 0.71073Å) and collimating mirror monochromators was used to collect XRD data. 2103 frames of data were collected using Omega scan with a scan range of 1º and a counting time of 1 s per frame.

The measured SCXRD data were used to solve the crystal structure and refine the atomic positions of the stishovite or post-stishovite phase at high pressure following a previous SCXRD processing method (Bykova, 2015). At a given pressure, we initially used CrysAlis^{PRO} software to find unit cell, determine lattice parameters, extract intensity for each hkl reflection, and perform absorption corrections for each crystal (Rigaku, 2015). The reflection datasets from the three stishovite crystals were combined for the further analysis. JANA software was then used to determine the space group, resolve structure using a charge-flipping algorithm, and refine atomic coordinates and isotropic/anisotropic displacement parameters of the crystal (Petříček et al., 2014). On the other hand, the stishovite structure at ambient conditions was solved by direct methods and

This is the peer-reviewed, final accepted version for American Mineralogist, published by the Mineralogical Society of America.
The published version is subject to change. Cite as Authors (Year) Title. American Mineralogist, in press.
DOI: https://doi.org/10.2138/am-2022-8458. http://www.minsocam.org/

then refined together with anisotropic displacement parameters of Si and O atoms using SHELXL software (Sheldrick, 2015). Structural analysis of the Si and O atomic positions, bond lengths and bond angles was evaluated using the programs PLATON (Spek, 2009) and OLEX2 at ambient conditions (Dolomanov et al., 2009). The quality of the refinements at each pressure were evaluated by residual *R*-factors such as R_{int} and R_1 (Bykova, 2015). The refined parameters of the crystal structure were viewed and graphed using VESTA software (Momma and Izumi, 2011).

The refined structural parameters were further used to perform distortion mode analysis across the post-stishovite transition using AMPLIMODES program (Orobengoa et al., 2009). The program is used to evaluate symmetry-adapted structural distortion between high- and low-symmetry phases across a displacive phase transition. Our input high-symmetry structural data are refined lattice parameters and atomic positions of stishovite at ambient conditions, while input low-symmetry data are those of stishovite and post-stishovite phases at high pressure. The AMPLIMODES program is used to calculate the maximum atomic displacement and global structural distortion in the distorted low-symmetry structure relative to the reference high-symmetry structure (Perez-Mato et al., 2010). The program then decomposes the global distortion into different symmetry-adapted distortion modes. Amplitude of the individual mode can reflect its contribution to the global structural distortion (Gawryluk et al., 2019).

RESULTS

Crystallographic analysis

Analysis of the collected SCXRD images shows that reflection spots of the three crystals display a round shape with a full-width at half maximum (FWHM) of less than 0.1º. The FWHM is almost invariant up to 75.3 GPa, indicating that the single-crystal quality of stishovite was

preserved in compression in neon medium (Yamanaka et al., 2002) (Figures 1c and 1d). We observed 66 to 239 total reflections from the crystals at high pressure (Figures 1a and 1b). These reflections were then grouped into 31 to 55 unique reflections which were used to determine lattice parameters at high pressure (Table 1). Furthermore, 24 to 63 reflections of $I > 3\sigma(I)$, where I is the intensity and σ is the standard deviation, were used to determine the space group and to refine atomic positions of the crystal at high pressure. Our analyses show that the crystal is in the tetragonal stishovite structure with $P4_2/mnm$ (No. 136) space group at pressures up to 49.8 GPa (Figures S2 and S3; Tables 1 and S1). From 52.4 GPa to 75.3 GPa, the crystal is stable in an orthorhombic structure with *Pnnm* (No. 58) space group, called the $CaCl_2$-type post-stishovite phase (Figures S2 and S3; Tables 1 and S1). These results indicate that the post-stishovite phase transition occurs between 49.8 and 52.4 GPa, consistent with previous studies (Andrault et al., 1998; Hemley et al., 2000; Kingma et al., 1995; Zhang et al., 2021). Values of R_{int} and R_1 are 0.6-14.9% and 1.3-9.4%, respectively, indicating the refined crystal structures are of good quality (Table 1).

Atomic coordinates, bond lengths, and bond angles can be derived from the refined crystal structures (Figures 2 and 3; Table 2). Using Si atom positions in the stishovite structure as the reference, the x (or y) coordinate of oxygen relative to the Si positions changes slightly from 0.306 at ambient conditions to 0.303 at 49.8 GPa (Figures 2a and 3a). Crossing into the post-stishovite phase, the x coordinate of oxygen drastically decreases from 0.303 at 52.4 GPa to 0.279 at 75.3 GPa whereas the y coordinate drastically increases from 0.303 to 0.323 (Figure 3a). This splitting of oxygen coordinates corresponds to a splitting of a- and b-axis in the post-stishovite phase (Figure S2a). On the other hand, the Si-O bond lengths decrease continuously with increasing pressure up to 75.3 GPa (Figures 2 and 3b). The apical Si-O3 bond length is

initially much longer than the equatorial Si-O1(2) bond length at ambient conditions, but it decreases with increasing pressure much faster than the equatorial Si-O1(2) bond length. This anisotropic linear incompressibility behavior leads to an equal bond length of 1.703 Å for the two Si-O bonds at ~51.4 GPa where the post-stishovite transition occurs (Figures 3b). In the post-stishovite structure, the apical Si-O3 bond becomes shorter than the equatorial Si-O1(2) bond (Figures 2b and 3b). Additionally, the bond angles between Si and O atoms in the stishovite structure are almost unaffected by increasing pressure up to ~51 GPa: ∠O1(2)-Si-O3 = 90º, ∠O1-Si-O2 = ~81.3º, and ∠O1(2)-Si-O1(2) = ~98.7º (Figure 3c). Crossing into the post-stishovite phase, the bond angles are slightly changed: ∠O1-Si-O2 increases by 0.5º, ∠O1(2)-Si-O1(2) decreases by 0.5º, and ∠O1-Si-O3 or ∠O2-Si-O3 remains almost unchanged within uncertainties (~0.1º) up to 75.3 GPa. Accordingly, the O1-O2 interatomic distance remains unchanged under compression whereas the O1(2)-O1(2), O1-O3, and O2-O3 distances decrease with increasing pressure and the difference between O1-O3 and O2-O3 distance is negligible (Figure S4).

The aforementioned structural parameters are used to further analyze the volume, deformation, and rotation of the SiO_6 octahedron across the post-stishovite transition (Figures 2 and 4; Table 3). These analyses show that the SiO_6 volume decreases continuously with increasing pressure up to 75.3 GPa, resulting in a continuous decrease of the unit-cell volume (Figures S2b and S5). The deformation of SiO_6 octahedron can be quantitatively determined by the distortion index and the bond angle variance based on the refined bond lengths and bond angles, respectively. The distortion index is defined as $D\ (\%) = \frac{100}{6}\sum_{n=1}^{6}|l_i - l_{av}|/l_{av}$ where l_i is the Si-O bond length and l_{av} is the average Si-O bond length (Renner and Lehmann, 1986). The bond angle variance is defined as $\sigma^2(\mathrm{deg}^2) = \frac{1}{11}\sum_{i=1}^{12}(\alpha_i - 90°)^2$ where α_i is the O-Si-O bond angle (Robinson et

al., 1971). In the stishovite phase, the distortion index decreases from 1.3% at ambient pressure to zero at ~51.4 GPa whereas the bond angle variance remains invariant at approximately 27 deg^2 with increasing pressure up to ~51.4 GPa (Figures 4a and 4b). Crossing into the post-stishovite phase, the distortion index increases to approximately 0.3% whereas the bond angle variance decreases to approximately 24 deg^2 at ~75 GPa (Figures 4a and 4b). On the other hand, the rotation of the SiO_6 octahedron about the *c* axis can be evaluated with respect to the stishovite structure using a formula, $\Phi\ (°) = 45° - \arctan(ax_O/by_O)$, where y_O and x_O are the *y*- and *x*-coordinate of oxygen atoms, respectively (Bärnighausen et al., 1984; Range et al., 1987) (Figure 4c). These analyses show that the SiO_6 octahedron does not rotate in the stishovite phase but starts to rotate about the *c* axis crossing into the post-stishovite phase. At 75.3 GPa, the SiO_6 octahedral rotation is about 5.4º.

Our structural refinement results for stishovite are, for the first order, consistent with previous SCXRD studies up to 30 GPa (Hill et al., 1983; Ross et al., 1990; Sinclair and Ringwood, 1978; Sugiyama et al., 1987; Yamanaka et al., 2002) (Figures 3 and 4). Additionally, our results across the post-stishovite transition are generally consistent with a PXRD study using the Rietveld structural analysis (Andrault et al., 1998), except for the octahedral volume (Figure S5). We note that our SCXRD data have much higher resolutions and are denser in the vicinity of the transition pressure such that detailed structural evolutions are clearly revealed across the post-stishovite transition. On the other hand, comparisons between ab initio calculations and experimental results show very large discrepancies in the structural parameters especially for the post-stishovite phase (Figures 3 and 4). For example, theoretical calculations show equal equatorial and apical Si-O bond lengths in the post-stishovite structure at high pressure (Karki et al., 1997b), which is contrary to our results. This could be due to difficulties in properly

optimizing spontaneous strains in the post-stishovite phase to account for exchange-correlation interactions in the local-density approximation (LDA). This in turn can affect accuracy in theoretically-predicted elastic moduli across the ferroelastic post-stishovite transition which are quite different from experimentally-derived elastic moduli (Karki et al., 1997a; Yang and Wu, 2014; Zhang et al., 2021). Our study here not only provides reliable structural models of the stishovite and post-stishovite phases, but also serves as benchmarks for future ab initio calculations.

Distortion mode analysis

As shown in the previous section, the stishovite phase has the space group of $P4_2/mnm$ while the post-stishovite phase has the space group of *Pnnm*, revealing a group-subgroup relationship between these two space groups across the transition. In other words, the low-symmetry post-stishovite structure can be considered as the high-symmetry stishovite structure undergoing a symmetry-adapted lattice distortion. Therefore, analysis of the symmetry mode is another useful way to describe crystal structures in terms of the displacement of a set of atoms that are related by a given symmetry, as compared to standard crystallographic descriptions in terms of individual bond length and bond angle. Particularly, amplitude of symmetry modes represents magnitude of lattice distortions with different symmetry representations. This information can thus help better understand symmetry-adapted structure distortions across the ferroelastic post-stishovite transition.

Using the refined structural data from our study, we have calculated maximum atomic displacements and distortion mode amplitudes in a distorted crystal structure at a given pressure with respect to the reference structure at ambient conditions (Figure 5 and Table 4). The

displacement of Si atoms remains zero at high pressure because they remain stationary at (0, 0, 0) coordinate in the lattice. The displacement of oxygen atoms increases linearly from zero at ambient conditions to 0.022 Å at ~51.4 GPa. The oxygen atoms then start to move significantly upon further compression with the maximum atomic displacement of 0.1343 Å at 75.3 GPa (Figure 5a). This atomic displacement results in an occurrence of two symmetry-related distortion modes: GM_1^+ and GM_2^+ (Figure 5b). GM_1^+ is an in-plane stretching mode acting on the oxygen atoms (Figure 5c). Its amplitude increases linearly with pressure across the post-stishovite transition up to 0.0609 Å at 75.3 GPa. The GM_2^+ mode, which is related to oxygen rotations about *c* axis (Figure 5d), emerges at ~51.4 GPa. Its amplitude increases significantly with pressure and is much larger than that of GM_1^+ (e.g., 0.2616 Å at 75.3 GPa). These results therefore reveal that the stishovite phase undergoes an in-plane stretching distortion at high pressure while a rotational distortion becomes dominant in the post-stishovite structure.

DISCUSSION

Our single-crystal X-ray diffraction refinements on the refined Si and O coordinates, Si-O bond lengths, and O-Si-O bond angles across the post-stishovite transition can be used to correlate with previous elasticity and Landau modeling studies to shed new light on the pseudo-proper type ferroelastic transition (Carpenter et al., 2000; Hemley et al., 2000; Zhang et al., 2021). Firstly, we co-plot Si-O bond length difference and elastic properties at given experimental pressures (Figure 6). The elastic moduli of stishovite and post-stishovite are taken from a recent study that derived the moduli from measured sound velocities using combined Brillouin and impulsive stimulated light scattering techniques at high pressure (Zhang et al., 2021). The elastic modulus C_{11} increases with decreasing Si-O bond length difference but

flattens when the difference is below 0.01 Å, while C_{12} increases significantly across the transition (Figure 6a). As a result, the elastic modulus $(C_{11} - C_{12})/2$, which reflects the strain response to the shear stress along the [110] direction in the stishovite structure (Bell and Rupprecht, 1963), becomes zero when the apical and equatorial Si-O bond lengths become equal due to the stretching displacement of oxygen atoms in the GM_1^+ mode (Figures 5b and 5c). Accordingly, $C_{11} - C_{12}$, one of Born criteria of the tetragonal stishovite phase, becomes zero at the phase transition (Zhang et al., 2021). Crossing into the post-stishovite phase, C_{11} splits into C_{11} and C_{22} as the oxygen coordinates split (Figures 3a and 6a). As the equatorial Si-O1(2) bond length becomes longer than the apical Si-O3 bond length with increasing amplitude of the GM_1^+ stretching mode, the elastic moduli C_{11}, C_{22}, and C_{12} of the post-stishovite phase increase (Figures 5a and 6a). The corresponding Born criterion, $C_{11}C_{22} - C_{12}^2$, becomes positive in the post-stishovite phase, indicating its stability after the crossover of the equatorial and apical Si-O bond lengths.

The ferroelastic post-stishovite transition is also manifested by vanishing the shear wave $V_{S1[110]}$ (Zhang et al., 2021). $V_{S1[110]}$ decreases from 5.5 km/s to zero as the Si-O bond length difference decreases from 0.05 Å to zero (Figure 6b). We should note that the strong reduction of $V_{S1[110]}$ starts from ~40 GPa where the Si-O bond length difference becomes lower than ~0.01 Å. This non-linear pressure dependence of elasticity is one important consequence of the pseudo-proper typed ferroelastic transition in stishovite whose transition mechanism is the softening of the B_{1g} mode (Carpenter and Salje, 1998). The Si-O bond lengths represent the bonding strength of the lattice that determines the frequency of the optic mode. Previous Raman shift data and a pseudo-proper typed Landau model have shown that squared Raman shift of the B_{1g} mode (ω^2) is proportional to pressure (Carpenter et al., 2000; Hemley et al., 2000; Kingma et al., 1995). That

This is the peer-reviewed, final accepted version for American Mineralogist, published by the Mineralogical Society of America.
The published version is subject to change. Cite as Authors (Year) Title. American Mineralogist, in press.
DOI: https://doi.org/10.2138/am-2022-8458. http://www.minsocam.org/

is, $\omega^2 \propto P$ or $\omega \propto \sqrt{P}$. This non-linear relation in the Raman shift of the soft B_{1g} mode with respect to pressure can thus lead to the non-linear behavior in the shear velocity reduction close to the post-stishovite transition pressure. Across into the post-stishovite phase, $V_{S1[110]}$ increases as the Si-O bond length difference increases (Figure 6b).

We also use the structural parameters to quantify the spontaneous strains (e_1 and e_2) and order parameter Q in a pseudo-proper type Landau model at high pressure (Figure 7). The splitting of oxygen coordinates leads to a symmetry reduction from tetragonal to orthorhombic structure and an occurrence of the GM_2^+ rotational mode. Because $y_O > x_O$ in the orthorhombic post-stishovite phase (Figure 3a), the *a* axis becomes shorter whereas the *b* axis becomes longer with respect to the ideal stishovite structure. All these lead to the occurrence of a negative spontaneous strain e_1 and a positive spontaneous strain e_2 (Figure 7a). Additionally, as the amplitude of GM_2^+ significantly increases (Figure 5a), the SiO_6 octahedron rotates about the *c* axis in the post-stishovite structure (Figure 7a). Our results further show that the symmetry-breaking strain e_1 - e_2, whose eigenvalue is the aforementioned elastic modulus $C_{11} - C_{12}$, can be quantified by the SiO_6 rotation angle Φ (Figure 7b). That is, e_1 - e_2 is proportional to Φ. Because the order parameter Q is coupled linearly to the strain e_1 - e_2 (Carpenter et al., 2000), Q also changes linearly with Φ (Figure 7c). We should note that the value of Q is obtained from a set of Landau parameters that were derived from combined experimental elastic moduli, lattice parameters, and Raman shift data (Zhang et al., 2021).

These crystallographic data and symmetry mode results can be correlated with Landau modeling parameters to have a better understanding of the transition. Previous studies have shown that the post-stishovite transition belongs to the pseudo-proper type which is driven by the soft B_{1g} optic mode (Carpenter et al., 2000; Kingma et al., 1995). The Raman active B_{1g} mode

This is the peer-reviewed, final accepted version for American Mineralogist, published by the Mineralogical Society of America.
The published version is subject to change. Cite as Authors (Year) Title. American Mineralogist, in press.
DOI: https://doi.org/10.2138/am-2022-8458. http://www.minsocam.org/

represents a rotational vibration of oxygen atoms about the *c* axis (Hemley et al., 1986; Traylor et al., 1971). As the two Si-O bond lengths cross over each other due to an in-plane stretching of oxygen atoms with GM_1^+ symmetry (Figures 3b, 5b, and 5c), the Raman shifts of the B_{1g} optic mode decrease and would become zero at the critical pressure (P_C = 110.2 GPa) (Kingma et al., 1995; Zhang et al., 2021). However, the transition occurs at a much lower pressure of ~51.4 GPa where the two Si-O bond lengths are equal (Figure 3b). The oxygen coordinates split across the transition (Figure 3a), leading to a symmetry breaking from the point group 422 to 222 where one 4-fold axis becomes a 2-fold axis. This symmetry reduction further results in the occurrence of the GM_2^+ rotational mode and the SiO_6 octahedron rotation about the *c* axis. As a result, symmetry-breaking spontaneous strains appear. The eigenvalue $C_{11} - C_{12}$ and acoustic velocity $V_{S1[110]}$ accordingly vanish at the transition, leading to significant shear wave velocity softening (Zhang et al., 2021). Therefore, the Si-O bond lengths and SiO_6 octahedron rotation, together with their relevant GM_1^+ and GM_2^+ distortion modes, play a key role in the ferroelastic transition from the stishovite to the post-stishovite phase.

IMPLICATIONS

As discussed in the introduction, pseudo-proper, proper, and improper typed ferroelastic transitions can occur in representative naturally occurring silicate minerals in Earth's deep crust and mantle. The ferroelastic transitions are manifested by appearance of the symmetry-breaking spontaneous strain in the low-symmetry ferroelastic phase, although the driving force is different among these ferroelastic transitions (Wadhawan, 1982). Our study on the post-stishovite transition, a typical pseudo-proper typed ferroelastic transition, reveals the relationship between the macroscopic spontaneous strain and microscopic structural angle. Previous studies on proper

and improper typed transitions have also shown a similar relationship. For example, albite ($NaAlSi_3O_8$ feldspar) undergoes a proper typed ferroelastic transition from monoclinic (space group: $C2/m$) to triclinic (space group: $C\bar{1}$) structure at approximately 1300 K (Salje, 1985; Salje et al., 1985). The spontaneous strain e_4 varies linearly with -cos α where α is the lattice constant angle (Carpenter et al., 1998; Kroll et al., 1980). Improper typed ferroelastic transition occurs in CaPv from cubic to tetragonal phase at approximately 450 K and 12 GPa with the tetragonal shear strain proportional to the squared rotation angle of the SiO_6 octahedron about the c axis (Φ_{Pv}^2) (Kurashina et al., 2004; Sun et al., 2016; Zhao et al., 1993a; Zhao et al., 1993b). These results reveal that the symmetry-breaking strain occurs as the primary effect from the structural angle in the low-symmetry ferroelastic phase. Furthermore, the structural angles can be linked to given symmetry-adapted distortion modes based on a group-subgroup relation. For example, considering that CaPv has a parent structure with $Pm\bar{3}m$ space group and a low symmetry phase with the subgroup $I4/mcm$, the Φ_{Pv} angle can be attributed to a distortion mode with symmetry R_4^+ (Perez-Mato et al., 2010). Therefore, the change of the structural angle with the occurrence of symmetry-breaking distortion mode is an important consequence of the ferroelastic transition. Our results here can be combined with sound velocity and elastic moduli studies across the three types of ferroelastic transitions in silicates and oxides at high pressure. This helps shed light on the abnormal seismic properties across the transitions especially in the subducting slabs and deep crustal regions.

ACKNOWLEDGEMENTS

We thank Vincent Lynch for his assistance on SCXRD measurements at ambient conditions and data analysis. High-pressure SCXRD experiments were performed at 13ID-D, GSECARS.

FUNDING

GSECARS was supported by the National Science Foundation (EAR-0622171). This research used resources of the Advanced Photon Source, a U.S. Department of Energy (DOE) Office of Science User Facility operated for the DOE Office of Science by Argonne National Laboratory under Contract No. DE-AC02-06CH11357. Jung-Fu Lin acknowledges support from Geophysics Program of the U.S. National Science Foundation (EAR-1916941 and EAR-2001381) and the Joint-Use User Program of the Institute for Planetary Materials, Okayama University.

REFERENCES CITED

Aizu, K. (1969) Possible species of "ferroelastic" crystals and of simultaneously ferroelectric and ferroelastic crystals. Journal of the Physical society of Japan, 27(2), 387-396.

-. (1970) Determination of the state parameters and formulation of spontaneous strain for ferroelastics. Journal of the Physical Society of Japan, 28(3), 706-716.

Andrault, D., Angel, R.J., Mosenfelder, J.L., and Bihan, T.L. (2003) Equation of state of stishovite to lower mantle pressures. American Mineralogist, 88(2-3), 301-307.

Andrault, D., Fiquet, G., Guyot, F., and Hanfland, M. (1998) Pressure-induced Landau-type transition in stishovite. Science, 282(5389), 720-724.

Bärnighausen, H., Bossert, W., and Anselment, B. (1984) A second-order phase transition of calcium bromide and its geometrical interpretation. Acta Crystallographica Section A, 40.

Bell, R., and Rupprecht, G. (1963) Elastic constants of strontium titanate. Physical Review, 129(1), 90.

Birch, F. (1947) Finite elastic strain of cubic crystals. Physical review, 71(11), 809.

Boffa Ballaran, T., Kurnosov, A., and Trots, D. (2013) Single-crystal X-ray diffraction at extreme conditions: a review. High Pressure Research, 33(3), 453-465.

Brown, J., Abramson, E., and Angel, R. (2006) Triclinic elastic constants for low albite. Physics and Chemistry of Minerals, 33(4), 256-265.

Buchen, J., Marquardt, H., Schulze, K., Speziale, S., Boffa Ballaran, T., Nishiyama, N., and Hanfland, M. (2018) Equation of State of Polycrystalline Stishovite Across the Tetragonal-Orthorhombic Phase Transition. Journal of Geophysical Research: Solid Earth, 123(9), 7347-7360.

Bykova, E. (2015) Single-crystal X-ray diffraction at extreme conditions in mineral physics and material sciences.

Carpenter, M.A. (2006) Elastic properties of minerals and the influence of phase transitions. American mineralogist, 91(2-3), 229-246.

Carpenter, M.A., Hemley, R.J., and Mao, H.k. (2000) High-pressure elasticity of stishovite and the P42/mnm⇌ Pnnm phase transition. Journal of Geophysical Research: Solid Earth, 105(B5), 10807-10816.

Carpenter, M.A., and Salje, E.K. (1998) Elastic anomalies in minerals due to structural phase transitions. European Journal of Mineralogy, 693-812.

Carpenter, M.A., Salje, E.K., and Graeme-Barber, A. (1998) Spontaneous strain as a determinant of thermodynamic properties for phase transitions in minerals. European Journal of Mineralogy, 621-691.

Chariton, S., Bykov, M., Bykova, E., Koemets, E., Fedotenko, T., Winkler, B., Hanfland, M., Prakapenka, V.B., Greenberg, E., and McCammon, C. (2020) The crystal structures of Fe-bearing MgCO3 sp2- and sp3-carbonates at 98 GPa from single-crystal X-ray diffraction using synchrotron radiation. Acta Crystallographica Section E: Crystallographic Communications, 76(5), 715-719.

Clegg, W. (2019) The development and exploitation of synchrotron single-crystal diffraction for chemistry and materials. Philosophical Transactions of the Royal Society A, 377(2147), 20180239.

Dera, P. (2010) All different flavors of synchrotron single crystal X-ray diffraction experiments. High-pressure crystallography, p. 11-22. Springer.

Dolomanov, O.V., Bourhis, L.J., Gildea, R.J., Howard, J.A., and Puschmann, H. (2009) OLEX2: a complete structure solution, refinement and analysis program. Journal of applied crystallography, 42(2), 339-341.

Fei, Y., Ricolleau, A., Frank, M., Mibe, K., Shen, G., and Prakapenka, V. (2007) Toward an internally consistent pressure scale. Proceedings of the National Academy of Sciences, 104(22), 9182-9186.

Gawryluk, D., Klein, Y., Shang, T., Sheptyakov, D., Keller, L., Casati, N., Lacorre, P., Fernández-Díaz, M., Rodríguez-Carvajal, J., and Medarde, M. (2019) Distortion mode anomalies in bulk PrNiO 3: Illustrating the potential of symmetry-adapted distortion mode analysis for the study of phase transitions. Physical Review B, 100(20), 205137.

Harris, K.D., Tremayne, M., and Kariuki, B.M. (2001) Contemporary advances in the use of powder X-ray diffraction for structure determination. Angewandte Chemie International Edition, 40(9), 1626-1651.

Helffrich, G. (2006) Small-scale seismic heterogeneity and mantle structure. Astronomy & Geophysics, 47(1), 1.20-1.26.

Hemley, R., Mao, H.-K., and Chao, E. (1986) Raman spectrum of natural and synthetic stishovite. Physics and chemistry of Minerals, 13(5), 285-290.

Hemley, R., Shu, J., Carpenter, M., Hu, J., Mao, H., and Kingma, K. (2000) Strain/order parameter coupling in the ferroelastic transition in dense SiO2. Solid State Communications, 114(10), 527-532.

Hill, R., Newton, M., and Gibbs, G. (1983) A crystal chemical study of stishovite. Journal of Solid State Chemistry, 47(2), 185-200.

Ishii, T., Kojitani, H., and Akaogi, M. (2019) Phase Relations of Harzburgite and MORB up to the Uppermost Lower Mantle Conditions: Precise Comparison With Pyrolite by Multisample Cell High-Pressure Experiments With Implication to Dynamics of Subducted Slabs. Journal of Geophysical Research: Solid Earth.

Kaneshima, S. (2016) Seismic scatterers in the mid-lower mantle. Physics of the Earth and Planetary Interiors, 257, 105-114.

Karki, B.B., Stixrude, L., and Crain, J. (1997a) Ab initio elasticity of three high-pressure polymorphs of silica. Geophysical Research Letters, 24(24), 3269-3272.

Karki, B.B., Warren, M., Stixrude, L., Ackland, G., and Crain, J. (1997b) Ab initio studies of high-pressure structural transformations in silica. Physical Review B, 55(6), 3465.

Kingma, K.J., Cohen, R.E., Hemley, R.J., and Mao, H.-k. (1995) Transformation of stishovite to a denser phase at lower-mantle pressures. Nature, 374(6519), 243.

Kroll, H., Bambauer, H.U., and Schirmer, U. (1980) The high albite–monalbite and analbite–monalbite transitions. American Mineralogist, 65(11-12), 1192-1211.

Kurashina, T., Hirose, K., Ono, S., Sata, N., and Ohishi, Y. (2004) Phase transition in Al-bearing CaSiO3 perovskite: implications for seismic discontinuities in the lower mantle. Physics of the Earth and Planetary Interiors, 145(1-4), 67-74.

Lakshtanov, D.L., Sinogeikin, S.V., Litasov, K.D., Prakapenka, V.B., Hellwig, H., Wang, J., Sanches-Valle, C., Perrillat, J.-P., Chen, B., and Somayazulu, M. (2007) The post-stishovite phase transition in hydrous alumina-bearing SiO2 in the lower mantle of the earth. Proceedings of the National Academy of Sciences, 104(34), 13588-13590.

Litasov, K.D., Kagi, H., Shatskiy, A., Ohtani, E., Lakshtanov, D.L., Bass, J.D., and Ito, E. (2007) High hydrogen solubility in Al-rich stishovite and water transport in the lower mantle. Earth and Planetary Science Letters, 262(3), 620-634.

Liu, W., Yang, Y., Xia, Q., Ye, Y., Wang, Z., Zhang, P., and Li, G. (2018) Water decreases displacive phase transition temperature in alkali feldspar. European Journal of Mineralogy, 30(6), 1071-1081.

Momma, K., and Izumi, F. (2011) VESTA 3 for three-dimensional visualization of crystal, volumetric and morphology data. Journal of applied crystallography, 44(6), 1272-1276.

Niu, F., Kawakatsu, H., and Fukao, Y. (2003) Seismic evidence for a chemical heterogeneity in the midmantle: A strong and slightly dipping seismic reflector beneath the Mariana subduction zone. Journal of Geophysical Research: Solid Earth, 108(B9).

Orobengoa, D., Capillas, C., Aroyo, M.I., and Perez-Mato, J.M. (2009) AMPLIMODES: symmetry-mode analysis on the Bilbao Crystallographic Server. Journal of Applied Crystallography, 42(5), 820-833.

Pawley, A.R., McMillan, P.F., and Holloway, J.R. (1993) Hydrogen in stishovite, with implications for mantle water content. SCIENCE-NEW YORK THEN WASHINGTON-, 261, 1024-1024.

Perez-Mato, J., Orobengoa, D., and Aroyo, M. (2010) Mode crystallography of distorted structures. Acta Crystallographica Section A: Foundations of Crystallography, 66(5), 558-590.

Petříček, V., Dušek, M., and Palatinus, L. (2014) Crystallographic computing system JANA2006: general features. Zeitschrift für Kristallographie-Crystalline Materials, 229(5), 345-352.

Range, K.-J., Rau, F., Klement, U., and Heyns, A. (1987) β-PtO2: high pressure synthesis of single crystals and structure refinement. Materials research bulletin, 22(11), 1541-1547.

Renner, B., and Lehmann, G. (1986) Correlation of angular and bond length distortions in TO4 units in crystals. Zeitschrift für Kristallographie-Crystalline Materials, 175(1-2), 43-59.

Rigaku, O. (2015) Crysalis Pro. Rigaku Oxford Diffraction, Yarnton, England.

Robinson, K., Gibbs, G., and Ribbe, P. (1971) Quadratic elongation: a quantitative measure of distortion in coordination polyhedra. Science, 172(3983), 567-570.

Ross, N.L., Shu, J., and Hazen, R.M. (1990) High-pressure crystal chemistry of stishovite. American Mineralogist, 75(7-8), 739-747.

Rudnick, R., Gao, S., Holland, H., and Turekian, K. (2003) Composition of the continental crust. The crust, 3, 1-64.

Salje, E. (1985) Thermodynamics of sodium feldspar I: order parameter treatment and strain induced coupling effects. Physics and Chemistry of Minerals, 12(2), 93-98.

-. (1990) Phase transitions in ferroelastic and co-elastic crystals. Ferroelectrics, 104(1), 111-120.

539 Salje, E., Kuscholke, B., Wruck, B., and Kroll, H. (1985) Thermodynamics of sodium feldspar II:
540 experimental results and numerical calculations. Physics and Chemistry of Minerals, 12(2), 99-
541 107.
542 Salje, E.K. (1992) Application of Landau theory for the analysis of phase transitions in minerals. Physics
543 reports, 215(2), 49-99.
544 Sheldrick, G.M. (2015) Crystal structure refinement with SHELXL. Acta Crystallographica Section C:
545 Structural Chemistry, 71(1), 3-8.
546 Sinclair, W., and Ringwood, A. (1978) Single crystal analysis of the structure of stishovite. Nature,
547 272(5655), 714.
548 Spek, A.L. (2009) Structure validation in chemical crystallography. Acta Crystallographica Section D:
549 Biological Crystallography, 65(2), 148-155.
550 Sugiyama, M., Endo, S., and Koto, K. (1987) The crystal structure of stishovite under pressure up to 6
551 GPa. Mineralogical Journal, 13(7), 455-466.
552 Sun, N., Bian, H., Zhang, Y., Lin, J.-F., Prakapenka, V.B., and Mao, Z. (2020) High-Pressure Experimental
553 Study of Tetragonal CaSiO 3-Pervoskite to 200 GPa. AGU Fall Meeting Abstracts, 2020, p.
554 MR016-0011.
555 Sun, N., Mao, Z., Yan, S., Wu, X., Prakapenka, V.B., and Lin, J.F. (2016) Confirming a pyrolitic lower
556 mantle using self-consistent pressure scales and new constraints on CaSiO3 perovskite. Journal
557 of Geophysical Research: Solid Earth, 121(7), 4876-4894.
558 Thomson, A., Crichton, W., Brodholt, J., Wood, I., Siersch, N., Muir, J., Dobson, D., and Hunt, S. (2019)
559 Seismic velocities of CaSiO 3 perovskite can explain LLSVPs in Earth's lower mantle. Nature,
560 572(7771), 643-647.
561 Traylor, J.G., Smith, H., Nicklow, R., and Wilkinson, M. (1971) Lattice dynamics of rutile. Physical Review
562 B, 3(10), 3457.
563 Tsuchiya, T. (2011) Elasticity of subducted basaltic crust at the lower mantle pressures: Insights on the
564 nature of deep mantle heterogeneity. Physics of the Earth and Planetary Interiors, 188(3-4),
565 142-149.
566 Wadhawan, V.K. (1982) Ferroelasticity and related properties of crystals. Phase Transitions: A
567 Multinational Journal, 3(1), 3-103.
568 Waeselmann, N., Brown, J.M., Angel, R.J., Ross, N., Zhao, J., and Kaminsky, W. (2016) The elastic tensor
569 of monoclinic alkali feldspars. American Mineralogist, 101(5), 1228-1231.
570 Wang, W., Xu, Y., Sun, D., Ni, S., Wentzcovitch, R., and Wu, Z. (2020) Velocity and density characteristics
571 of subducted oceanic crust and the origin of lower-mantle heterogeneities. Nature
572 Communications, 11(1), 1-8.
573 Xu, F., Yamazaki, D., Sakamoto, N., Sun, W., Fei, H., and Yurimoto, H. (2017) Silicon and oxygen self-
574 diffusion in stishovite: Implications for stability of SiO2-rich seismic reflectors in the mid-mantle.
575 Earth and Planetary Science Letters, 459, 332-339.
576 Yamanaka, T., Fukuda, T., and Mimaki, J. (2002) Bonding character of SiO 2 stishovite under high
577 pressures up to 30 GPa. Physics and Chemistry of Minerals, 29(9), 633-641.
578 Yang, R., and Wu, Z. (2014) Elastic properties of stishovite and the CaCl 2-type silica at the mantle
579 temperature and pressure: An ab initio investigation. Earth and Planetary Science Letters, 404,
580 14-21.
581 Zhang, Y., Fu, S., Wang, B., and Lin, J.-F. (2021) Elasticity of a Pseudoproper Ferroelastic Transition from
582 Stishovite to Post-Stishovite at High Pressure. Physical Review Letters, 126(2), 025701.
583 Zhang, Z., and Klemperer, S.L. (2005) West-east variation in crustal thickness in northern Lhasa block,
584 central Tibet, from deep seismic sounding data. Journal of Geophysical Research: Solid Earth,
585 110(B9).

Zhao, W., Mechie, J., Brown, L., Guo, J., Haines, S., Hearn, T., Klemperer, S., Ma, Y., Meissner, R., and Nelson, K. (2001) Crustal structure of central Tibet as derived from project INDEPTH wide-angle seismic data. Geophysical Journal International, 145(2), 486-498.

Zhao, Y., Weidner, D.J., Parise, J.B., and Cox, D.E. (1993a) Critical phenomena and phase transition of perovskite—data for NaMgF3 perovskite. Part II. Physics of the Earth and Planetary Interiors, 76(1-2), 17-34.

-. (1993b) Thermal expansion and structural distortion of perovskite—data for NaMgF3 perovskite. Part I. Physics of the Earth and Planetary Interiors, 76(1-2), 1-16.

FIGURE 1. Representative single-crystal X-ray diffraction data of stishovite and post-stishovite at high pressure. (a) and (b) show original diffraction images at 28.5 GPa for stishovite and at 75.3 GPa for post-stishovite, respectively. Sample reflection spots are marked with red open circles. (c) An optical image of the sample chamber showing three crystals (P1, P2, and P3) and gold pressure calibrant (Au) in neon pressure medium (Ne) at 2.8 GPa. (d) Full-width at half maximum (FWHM) of a selected 101 diffraction peak as a function of pressure. FWHM of the peak (red solid circles) remains almost unchanged during compression. The insert panel shows a round 101 reflection spot and its integrated peak with FWHM of 0.07º at 75.3 GPa. These data indicate that the single crystal quality was preserved in compression up to 75.3 GPa.

FIGURE 2. Representative refined crystal structures of stishovite and post-stishovite at high pressure. (a) Stishovite at 49.8 GPa; (b) post-stishovite at 73.8 GPa. Silicon (Si) and oxygen (O1, O2, and O3) atoms are shown as blue and red balls, respectively. Lattice parameters, Si-O bond lengths, and O1-Si-O1 bond angles are labelled in the representative structures, and can also be found in Tables 1 and S1. Black arrows in (b) show Φ rotation angle of 5.1º which is the SiO_6 octahedron rotation about the *c* axis with respect to the ideal stishovite structure in (a).

FIGURE 3. Oxygen coordinates, Si-O bond lengths, and O-Si-O bond angles across the post-stishovite transition at high pressure. (a) Oxygen coordinates as a function of pressure. The *x* and *y* coordinates for oxygen are almost invariant in stishovite; however, *x* coordinate decreases and *y* coordinate increases with increasing pressure in the post-stishovite phase. (b) Si-O bond lengths as a function of pressure. The bond length in the apical Si-O3 and in the equatorial Si-O1(2) becomes equivalent to each other within uncertainties at the post-stishovite transition. (c) O-Si-O bond angles as a function of pressure. The angles remain almost constant in the stishovite phase, while ∠O1-Si-O2 increases and ∠O1(2)-Si-O1(2) decreases with increasing pressure in the post-stishovite phase. Please refer to Figure 2 for the meaning of the oxygen atom numbering. Solid lines in (b) show the best fits using an axial incompressibility equation of state (Birch, 1947), while those in (a) and (c) are the best polynomial fits to guide the eyes. Note that the data and fit for ∠O1-Si-O3 are drawn in green in order to distinguish it from ∠O2-Si-O3. The gray vertical band shows the phase transition region at ~51.4 GPa based on the splitting of the oxygen coordinates. Literature single-crystal and powder XRD and ab initio data are plotted

for comparison (Andrault et al., 1998; Hill et al., 1983; Karki et al., 1997b; Ross et al., 1990; Sinclair and Ringwood, 1978; Sugiyama et al., 1987; Yamanaka et al., 2002).

FIGURE 4. Refined SiO_6 octahedron parameters of stishovite and post-stishovite at high pressure. (a) Bond length distortion (D) of the octahedron as a function of pressure. The distortion vanishes at the transition. (b) Angle variance (σ^2) of the octahedron as a function of pressure. It remains constant in stishovite but decreases with increasing pressure in the post-stishovite phase. (c) The rotation of the SiO_6 octahedron about the c axis (Φ) with pressure only occurs in the post-stishovite phase (also see Figure 2 for the rotation). Lines show the best polynomial fits to the data. The gray vertical band represents the transition pressure. Previous studies are also shown for comparison (Andrault et al., 1998; Hill et al., 1983; Karki et al., 1997b; Ross et al., 1990; Sinclair and Ringwood, 1978; Sugiyama et al., 1987; Yamanaka et al., 2002).

FIGURE 5. Atomic displacements and distortion mode amplitudes across the post-stishovite transition at high pressure. (a) Maximum displacement of oxygen atoms in the crystal structure; (b) Amplitude of GM_1^+ and GM_2^+ distortion modes. Black lines are best linear or polynomial fits to guide the eyes. Atomic displacements for GM_1^+ and GM_2^+ are schematically drawn in (c) and (d), respectively. In (c) and (d), blue and red spheres represent silicon and oxygen atoms, respectively, shaded area represents a SiO_6 octahedron, and black lines with arrows represent atomic displacements upon compression.

FIGURE 6. Elastic moduli and shear wave velocity of stishovite and post-stishovite as a function of the bond length difference between the apical and equatorial Si-O bonds. (a) Selected elastic moduli, C_{11}, C_{12}, and C_{22}; (b) transverse shear wave $V_{S1[110]}$ polarizing along $[1\bar{1}0]$ and propagating along [110] direction. At a given pressure, elastic moduli and sound velocities are taken from Zhang et al. (2021) while bond length data are taken from refined atomic positions in this study and previous reports as shown in the legend (Andrault et al., 1998; Hill et al., 1983; Karki et al., 1997b; Ross et al., 1990; Sinclair and Ringwood, 1978; Sugiyama et al., 1987; Yamanaka et al., 2002). Note that bond length data from this study are shown in solid circles with different colors for figure clarity. Black lines show co-plotting of Landau modeling results

for the elastic properties in Zhang et al. (2021) and linear incompressibility fitting results for bond lengths in Figure 3b. When the apical bond length is equal to the equatorial bond length, C_{11} converges with C_{12} in (a) and $V_{S1[110]}$ vanishes in (b). The gray vertical band shows the post-stishovite phase transition region. Early studies are also plotted for comparison.

FIGURE 7. Landau parameters as a function of the SiO_6 rotation angle Φ about the *c* axis across the post-stishovite transition. (a) Schematics to highlight the rotation of the SiO_6 octahedron and the occurrence of the spontaneous strains e_1 and e_2 in (b). Blue and red spheres represent Si and O atoms, respectively. The *ab* plane of the post-stishovite unit cell is schematically drawn in the pink area with dashed lines, whereas the *aa* plane in the stishovite structure is shown in the blue area with solid lines for comparison for the lattice rotation. (b) Symmetry-breaking spontaneous strain e_1 - e_2 and (c) order parameter Q as a function of Φ. Crossing into the post-stishovite phase, e_1 - e_2 and Q emerge and increase linearly with Φ in (a) and (b), respectively. The gray vertical band shows the transition pressure. Literature data are plotted for comparison (Andrault et al., 1998; Hill et al., 1983; Ross et al., 1990; Sinclair and Ringwood, 1978; Sugiyama et al., 1987; Yamanaka et al., 2002).

This is the peer-reviewed, final accepted version for American Mineralogist, published by the Mineralogical Society of America.
The published version is subject to change. Cite as Authors (Year) Title. American Mineralogist, in press.
DOI: https://doi.org/10.2138/am-2022-8458. http://www.minsocam.org/

736 **TABLE 1.** Structure refinement results for stishovite and post-stishovite at high pressure

P, GPa	space group	*a*, Å	*b*, Å	*c*, Å	*V*, Å^3	unique refl[1]	R_{int}, %	R_1, %
0	$P4_2/mnm$	4.1752(1)		2.6642(1)	46.443(3)	2788	4.63	1.29
2.8(1)	$P4_2/mnm$	4.1660(3)		2.6640(3)	46.24(1)	55	0.61	3.48
7.8(1)	$P4_2/mnm$	4.1416(5)		2.6564(3)	45.57(1)	48	1.52	5.93
13.0(2)	$P4_2/mnm$	4.1200(4)		2.6458(3)	44.91(1)	37	0.78	6.28
16.0(1)	$P4_2/mnm$	4.1066(4)		2.6433(4)	44.58(1)	50	5.89	6.14
16.9(3)	$P4_2/mnm$	4.1045(4)		2.6393(3)	44.464(8)	48	0.35	6.11
19.7(1)	$P4_2/mnm$	4.0891(4)		2.6298(17)	43.97(3)	50	1.65	3.78
21.4(1)	$P4_2/mnm$	4.0875(4)		2.6366(3)	44.05(1)	41	12.74	6.00
26.8(2)	$P4_2/mnm$	4.0681(5)		2.6259(5)	43.46(1)	43	4.37	7.84
28.5(2)	$P4_2/mnm$	4.0520(4)		2.6162(18)	42.95(3)	52	1.70	7.73
33.8(2)	$P4_2/mnm$	4.0318(6)		2.6070(8)	42.38(2)	48	5.80	6.17
40.4(2)	$P4_2/mnm$	4.0133(7)		2.6000(30)	41.88(5)	34	8.91	5.61
48.7(2)	$P4_2/mnm$	3.9875(7)		2.5840(30)	41.09(5)	46	1.06	5.65
49.8(2)	$P4_2/mnm$	3.9819(10)		2.5810(60)	40.92(10)	36	1.01	5.35
52.4(2)	*Pnnm*	3.9440(30)	4.0150(19)	2.5851(13)	40.93(4)	47	1.25	5.66
54.2(2)	*Pnnm*	3.9320(30)	4.0128(18)	2.5817(12)	40.73(4)	56	0.87	5.38
55.6(2)	*Pnnm*	3.9300(40)	4.0097(10)	2.5750(5)	40.58(4)	54	4.82	6.22
58.6(3)	*Pnnm*	3.9140(50)	4.0118(12)	2.5717(6)	40.38(5)	31	14.89	4.97
62.0(3)	*Pnnm*	3.9010(40)	4.0089(12)	2.5656(8)	40.12(4)	41	2.94	6.88
64.4(3)	*Pnnm*	3.8880(40)	4.0080(20)	2.5681(14)	40.01(5)	46	4.80	6.66
65.8(3)	*Pnnm*	3.8820(40)	4.0070(10)	2.5667(8)	39.93(4)	41	12.90	6.62
68.0(3)	*Pnnm*	3.8710(40)	4.0051(10)	2.5616(7)	39.71(4)	41	1.40	6.85
71.0(3)	*Pnnm*	3.8580(30)	4.0040(9)	2.5580(7)	39.51(3)	46	1.91	4.57
73.8(3)	*Pnnm*	3.8500(30)	4.0016(8)	2.5557(6)	39.37(3)	45	2.60	6.05
75.3(3)	*Pnnm*	3.8380(20)	3.9974(7)	2.5498(5)	39.12(2)	46	0.55	4.42

[1]unique refl: number of unique observed reflections

737
738
739
740
741
742
743
744

This is the peer-reviewed, final accepted version for American Mineralogist, published by the Mineralogical Society of America.
The published version is subject to change. Cite as Authors (Year) Title. American Mineralogist, in press.
DOI: https://doi.org/10.2138/am-2022-8458. http://www.minsocam.org/

745 **TABLE 2.** Oxygen positions, bond lengths, and bond angles of stishovite and post-stishovite at
746 high pressure. Please refer to Fig. 2 for the meaning of the atom symbols.

P,GPa	oxygen position		bond length, Å		bond angle, º			
	x	y	Si-O3	Si-O1(2)	∠O1-Si-O3	∠O2-Si-O3	∠O1(2)-Si-O1(2)	∠O1-Si-O2
0	0.3061(1)	0.3061(1)	1.8075(6)	1.7565(4)	90.00(5)	90.00(5)	98.65(5)	81.35(5)
2.8(1)	0.3060(3)	0.3060(3)	1.803(1)	1.755(1)	90.00(7)	90.00(7)	98.74(7)	81.26(7)
7.8(1)	0.3052(5)	0.3052(5)	1.788(3)	1.751(1)	90.00(9)	90.00(9)	98.67(8)	81.33(8)
13.0(2)	0.3046(5)	0.3046(5)	1.775(3)	1.745(1)	90.00(9)	90.00(9)	98.57(8)	81.43(8)
16.0(1)	0.3046(5)	0.3046(5)	1.769(3)	1.742(1)	90.00(9)	90.00(9)	98.70(8)	81.30(8)
16.9(3)	0.3046(3)	0.3046(3)	1.7681(13)	1.7401(9)	90.00(9)	90.00(9)	98.64(8)	81.36(8)
19.7(1)	0.3039(5)	0.3039(5)	1.757(3)	1.736(2)	90.00(9)	90.00(9)	98.45(8)	81.55(8)
21.4(1)	0.3044(6)	0.3044(6)	1.760(3)	1.737(2)	90.00(10)	90.00(10)	98.76(9)	81.24(9)
26.8(2)	0.3048(6)	0.3048(6)	1.754(3)	1.728(2)	90.00(10)	90.00(10)	98.92(9)	81.08(9)
28.5(2)	0.3038(6)	0.3038(6)	1.741(3)	1.725(2)	90.00(10)	90.00(10)	98.64(9)	81.36(9)
33.8(2)	0.3036(4)	0.3036(4)	1.731(2)	1.719(1)	90.00(8)	90.00(8)	98.67(8)	81.33(8)
40.4(2)	0.3036(4)	0.3036(4)	1.7231(17)	1.7125(16)	90.00(10)	90.00(10)	98.78(9)	81.22(9)
48.7(2)	0.3028(5)	0.3028(5)	1.708(3)	1.705(2)	90.00(9)	90.00(9)	98.56(8)	81.44(8)
49.8(2)	0.3023(4)	0.3023(4)	1.702(2)	1.704(3)	90.00(8)	90.00(8)	98.43(8)	81.57(8)
52.4(2)	0.2943(12)	0.3106(5)	1.704(4)	1.705(3)	89.87(15)	90.13(15)	98.59(14)	81.41(14)
54.2(2)	0.2912(12)	0.3121(5)	1.697(4)	1.706(3)	89.92(15)	90.08(15)	98.38(14)	81.62(14)
55.6(2)	0.2927(7)	0.3127(6)	1.702(3)	1.6986(18)	89.91(12)	90.09(12)	98.57(11)	81.43(11)
58.6(3)	0.2877(12)	0.3152(6)	1.693(4)	1.701(3)	89.96(14)	90.04(14)	98.21(13)	81.79(13)
62.0(3)	0.2854(16)	0.3167(8)	1.689(5)	1.699(4)	89.98(16)	90.02(16)	98.06(15)	81.94(15)
64.4(3)	0.2850(14)	0.3175(7)	1.687(5)	1.698(4)	89.91(16)	90.09(16)	98.28(15)	81.72(15)
65.8(3)	0.2841(14)	0.3188(7)	1.688(5)	1.696(3)	89.94(15)	90.06(15)	98.34(15)	81.66(15)
68.0(3)	0.2814(12)	0.3200(6)	1.682(4)	1.696(3)	89.96(14)	90.04(14)	98.09(14)	81.91(14)
71.0(3)	0.2807(9)	0.3211(5)	1.681(3)	1.693(2)	89.90(12)	90.10(12)	98.17(12)	81.83(12)
73.8(3)	0.2794(12)	0.3216(6)	1.677(4)	1.692(3)	89.90(14)	90.10(14)	98.07(14)	81.93(14)
75.3(3)	0.2788(8)	0.3231(4)	1.677(3)	1.687(2)	89.90(11)	90.10(11)	98.17(11)	81.83(11)

747
748
749
750
751
752
753
754
755

This is the peer-reviewed, final accepted version for American Mineralogist, published by the Mineralogical Society of America.
The published version is subject to change. Cite as Authors (Year) Title. American Mineralogist, in press.
DOI: https://doi.org/10.2138/am-2022-8458. http://www.minsocam.org/

TABLE 3. Volume (V_{oct}), bond length distortion (D), angle variance (σ^2), and rotation angle about c axis (Φ) of the SiO_6 octahedron in the stishovite and post-stishovite phases at high pressure

P,GPa	V_{oct}, Å^3	D	σ^2, deg^2	Φ, º
0	7.351(2)	0.01278(3)	27.186(7)	0
2.8(1)	7.319(4)	0.01196(7)	27.75(2)	0
7.8(1)	7.224(8)	0.00923(10)	27.35(3)	0
13.0(2)	7.128(8)	0.00745(8)	26.70(3)	0
16.0(1)	7.075(8)	0.00685(8)	27.52(3)	0
16.9(3)	7.057(9)	0.00711(11)	27.16(3)	0
19.7(1)	6.988(8)	0.00537(6)	25.96(3)	0
21.4(1)	6.994(9)	0.00582(7)	27.92(3)	0
26.8(2)	6.895(8)	0.00662(8)	28.91(3)	0
28.5(2)	6.828(9)	0.00412(5)	27.16(3)	0
33.8(2)	6.738(5)	0.00325(3)	27.32(2)	0
40.4(2)	6.659(5)	0.00276(2)	28.01(2)	0
48.7(2)	6.542(8)	0.00075(1)	26.66(3)	0
49.8(2)	6.522(10)	0.00053(1)	25.85(4)	0
52.4(2)	6.530(13)	0.00036(4)	26.85(5)	2.1(2)
54.2(2)	6.511(13)	0.00225(1)	25.52(5)	2.6(2)
55.6(2)	6.473(8)	0.00076(1)	26.71(3)	2.5(1)
58.6(3)	6.466(13)	0.00204(4)	24.52(5)	3.3(2)
62.0(3)	6.435(16)	0.00270(7)	23.63(6)	3.8(2)
64.4(3)	6.418(18)	0.00274(11)	24.92(7)	4.0(2)
65.8(3)	6.405(14)	0.00221(5)	25.31(5)	4.2(2)
68.0(3)	6.386(13)	0.00366(7)	23.79(5)	4.6(2)
71.0(3)	6.356(9)	0.00304(4)	24.26(3)	4.9(1)
73.8(3)	6.341(13)	0.00396(8)	23.68(5)	5.1(2)
75.3(3)	6.300(8)	0.00259(3)	24.29(3)	5.4(1)

This is the peer-reviewed, final accepted version for American Mineralogist, published by the Mineralogical Society of America.
The published version is subject to change. Cite as Authors (Year) Title. American Mineralogist, in press.
DOI: https://doi.org/10.2138/am-2022-8458. http://www.minsocam.org/

767 **TABLE 4.** Maximum atomic displacement (Δ) and distortion mode amplitude at high pressure

P,GPa	Δ, Å	GM_1^+, Å	GM_2^+, Å
0	0.0000	0.0000	-
2.8(1)	0.0006(0)	0.0013(0)	-
7.8(1)	0.0054(1)	0.0107(2)	-
13.0(2)	0.0089(1)	0.0178(3)	-
16.0(1)	0.0089(1)	0.0178(3)	-
16.9(3)	0.0089(1)	0.0178(2)	-
19.7(1)	0.0125(1)	0.0249(2)	-
21.4(1)	0.0101(2)	0.0202(4)	-
26.8(2)	0.0077(2)	0.0155(3)	-
28.5(2)	0.0125(2)	0.0249(4)	-
33.8(2)	0.0148(2)	0.0296(4)	-
40.4(2)	0.0148(2)	0.0296(4)	-
48.7(2)	0.0195(3)	0.0391(6)	-
49.8(2)	0.0225(5)	0.0450(11)	-
52.4(2)	0.0528(18)	0.0432(14)	0.0962(32)
54.2(2)	0.0671(20)	0.0527(16)	0.1234(37)
55.6(2)	0.0624(15)	0.0403(10)	0.1181(28)
58.6(3)	0.0857(36)	0.0550(23)	0.1624(68)
62.0(3)	0.0971(54)	0.0598(34)	0.1848(104)
64.4(3)	0.1001(56)	0.0574(32)	0.1919(108)
65.8(3)	0.1061(52)	0.0550(27)	0.2049(101)
68.0(3)	0.1184(50)	0.0639(27)	0.2279(97)
71.0(3)	0.1232(40)	0.0615(20)	0.2385(76)
73.8(3)	0.1289(55)	0.0663(28)	0.2492(107)
75.3(3)	0.1343(39)	0.0609(17)	0.2616(75)

Note: distortion mode of GM_1^+ occurs in stishovite below ~50 GPa, while both GM_1^+ and GM_2^+ modes are present in post-stishovite above ~52 GPa.

768

769

770

This is the peer-reviewed, final accepted version for American Mineralogist, published by the Mineralogical Society of America.
The published version is subject to change. Cite as Authors (Year) Title. American Mineralogist, in press.
DOI: https://doi.org/10.2138/am-2022-8458. http://www.minsocam.org/

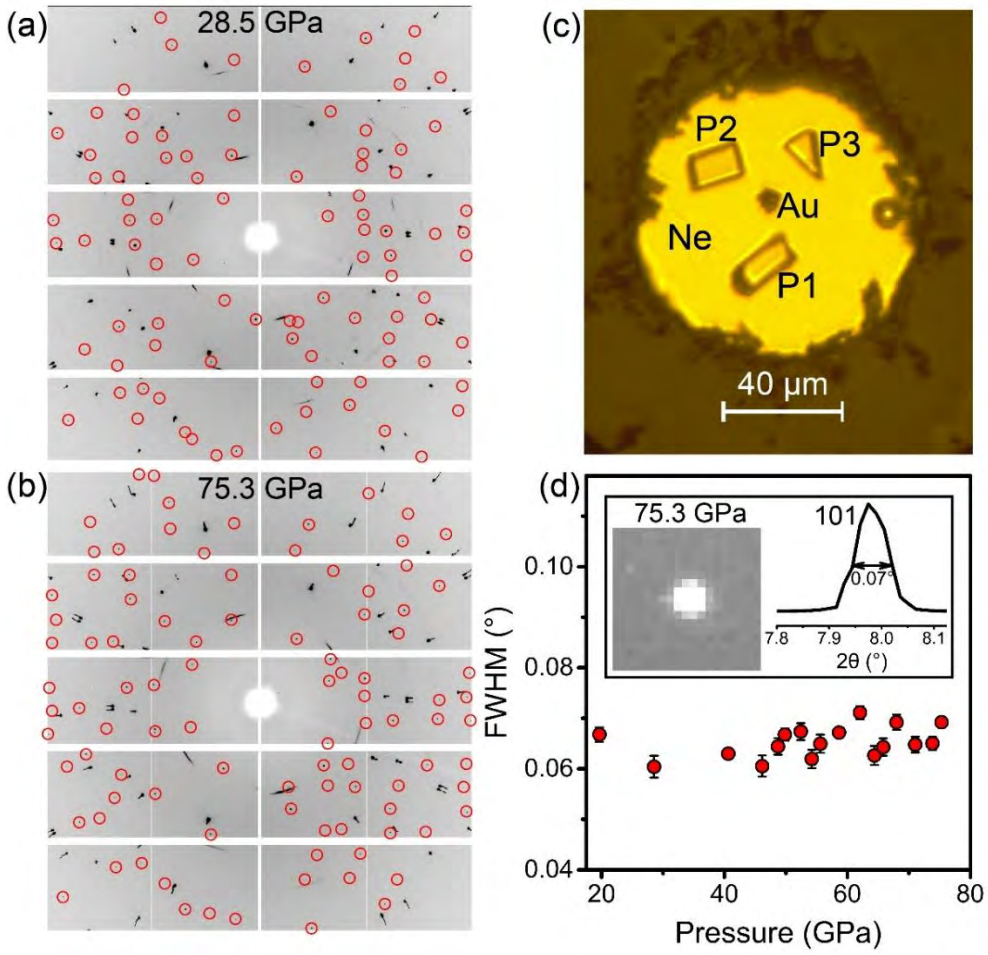

Fig 1

This is the peer-reviewed, final accepted version for American Mineralogist, published by the Mineralogical Society of America.
The published version is subject to change. Cite as Authors (Year) Title. American Mineralogist, in press.
DOI: https://doi.org/10.2138/am-2022-8458. http://www.minsocam.org/

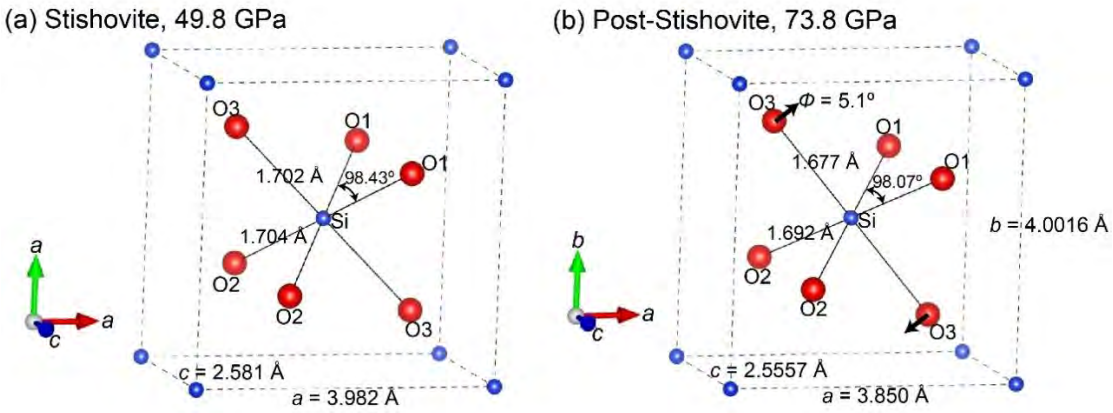

Fig 2

This is the peer-reviewed, final accepted version for American Mineralogist, published by the Mineralogical Society of America.
The published version is subject to change. Cite as Authors (Year) Title. American Mineralogist, in press.
DOI: https://doi.org/10.2138/am-2022-8458. http://www.minsocam.org/

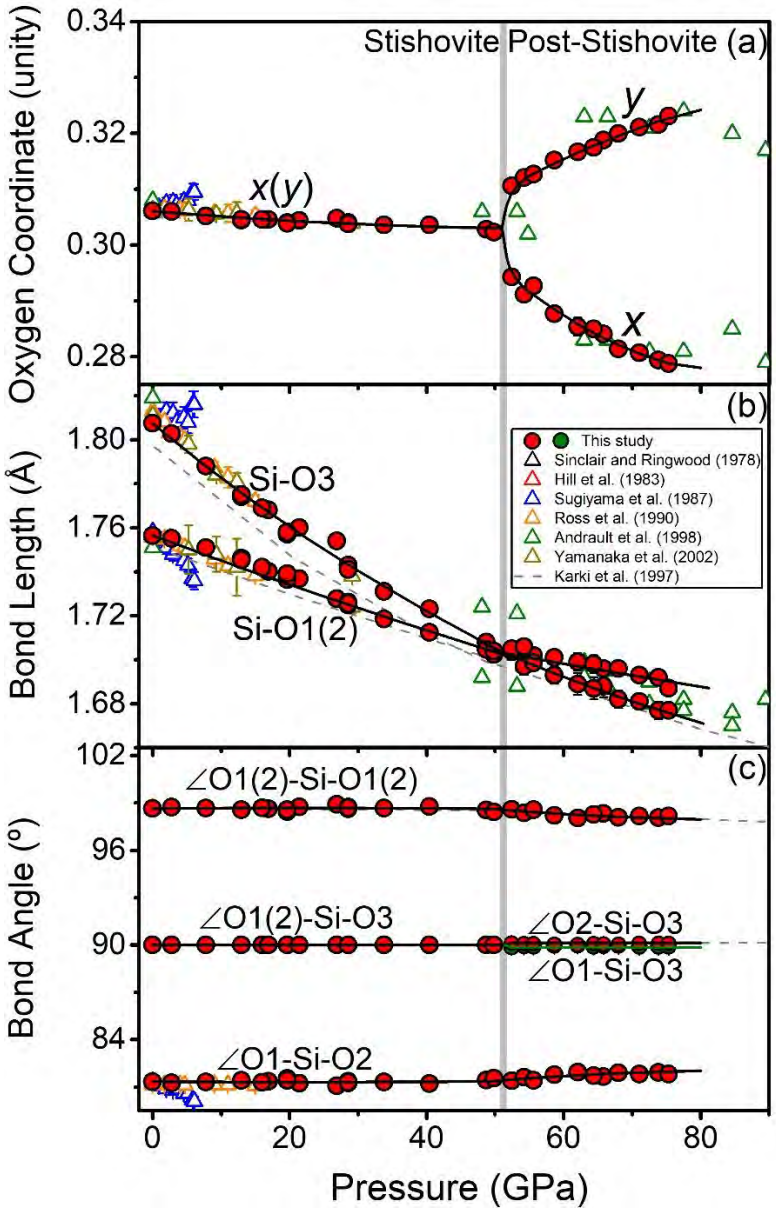

Fig 3

This is the peer-reviewed, final accepted version for American Mineralogist, published by the Mineralogical Society of America.
The published version is subject to change. Cite as Authors (Year) Title. American Mineralogist, in press.
DOI: https://doi.org/10.2138/am-2022-8458. http://www.minsocam.org/

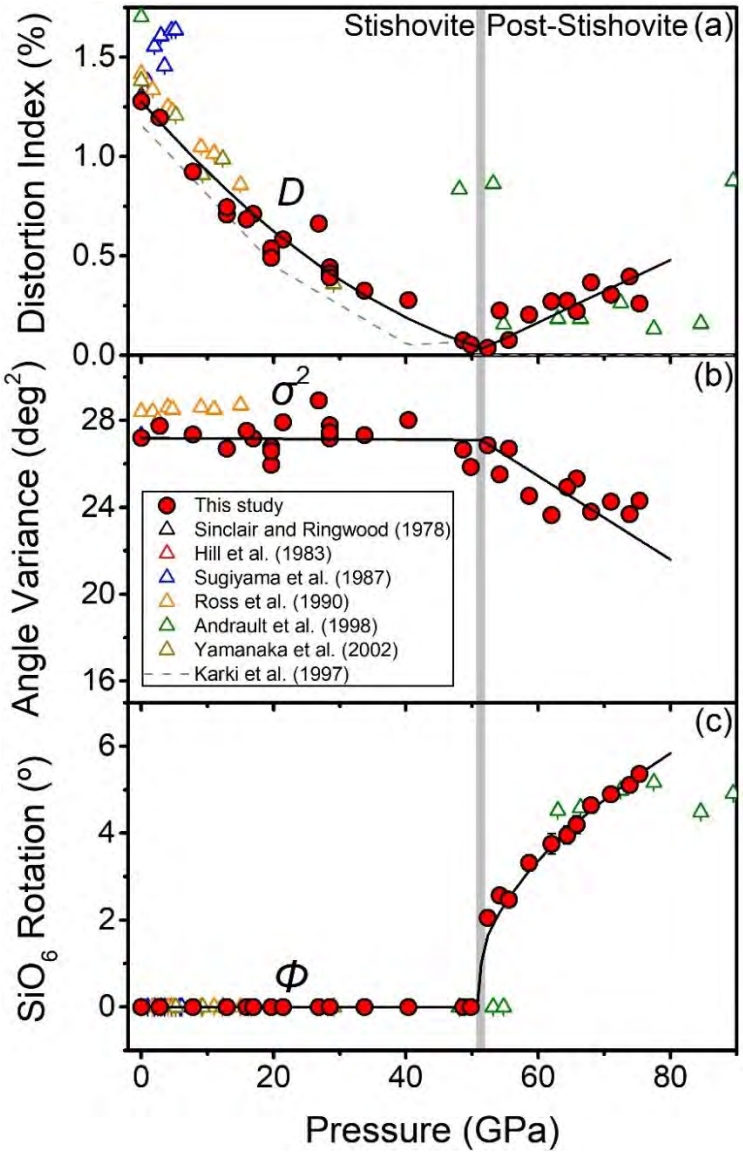

Fig 4

This is the peer-reviewed, final accepted version for American Mineralogist, published by the Mineralogical Society of America.
The published version is subject to change. Cite as Authors (Year) Title. American Mineralogist, in press.
DOI: https://doi.org/10.2138/am-2022-8458. http://www.minsocam.org/

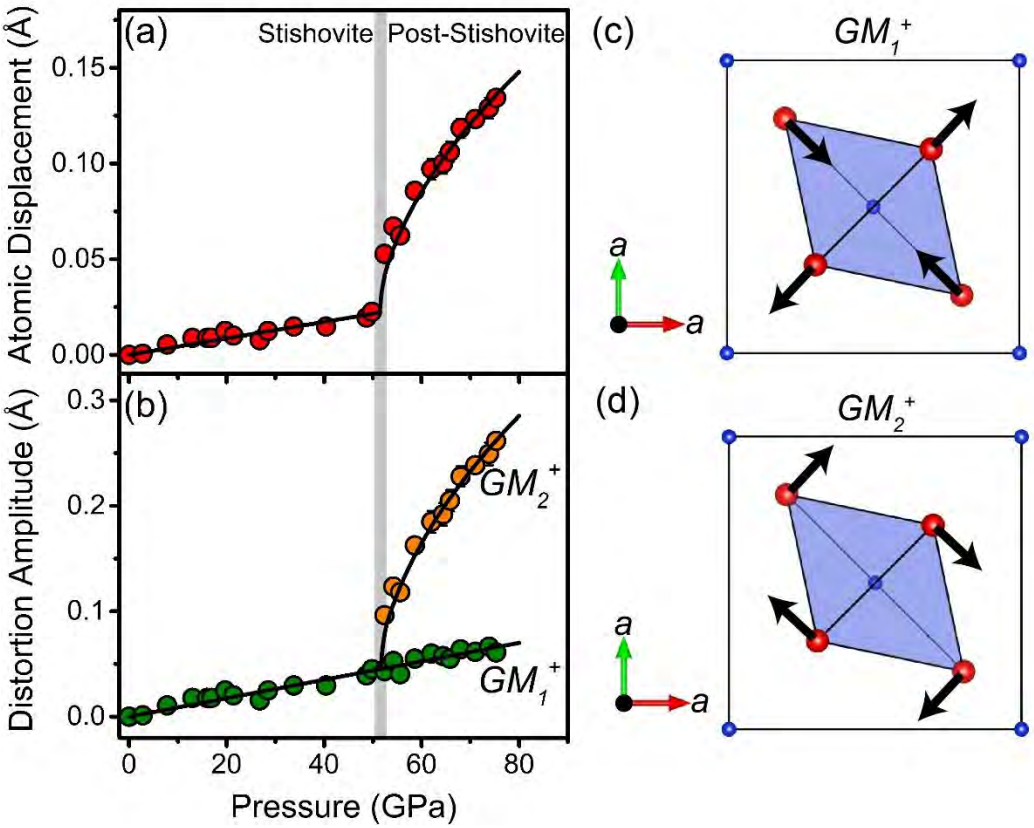

Fig 5

This is the peer-reviewed, final accepted version for American Mineralogist, published by the Mineralogical Society of America.
The published version is subject to change. Cite as Authors (Year) Title. American Mineralogist, in press.
DOI: https://doi.org/10.2138/am-2022-8458. http://www.minsocam.org/

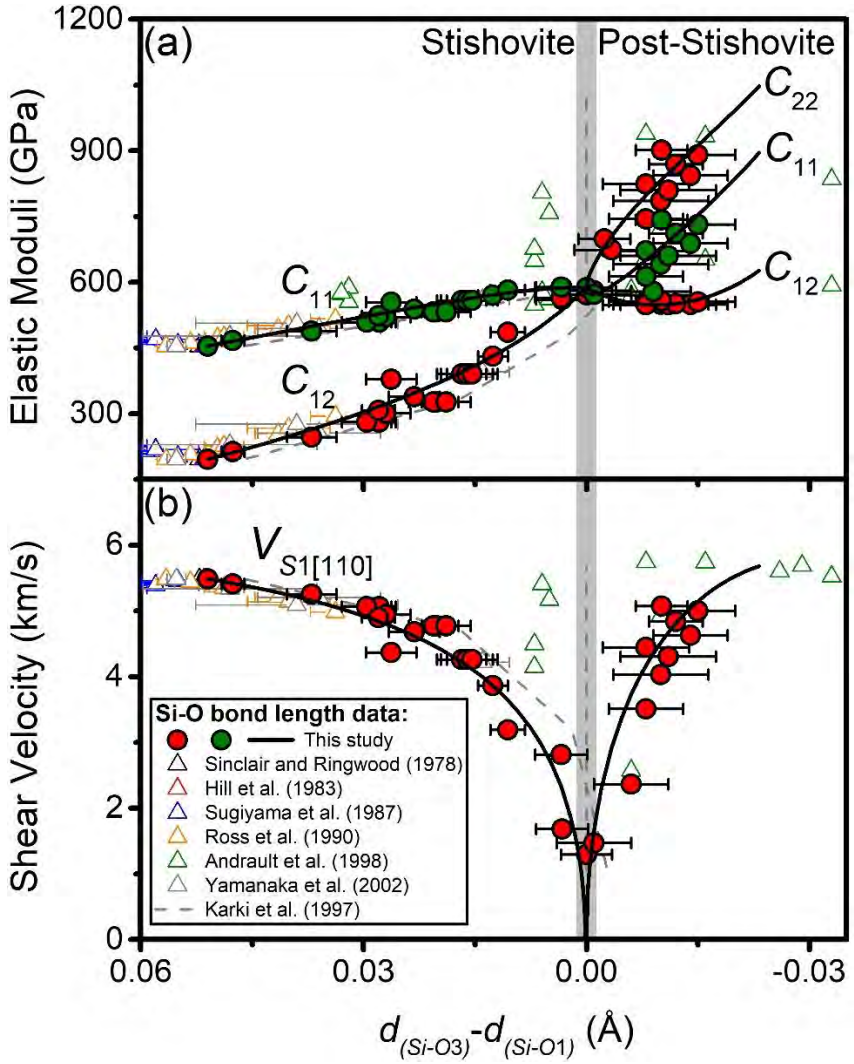

Fig 6

This is the peer-reviewed, final accepted version for American Mineralogist, published by the Mineralogical Society of America.
The published version is subject to change. Cite as Authors (Year) Title. American Mineralogist, in press.
DOI: https://doi.org/10.2138/am-2022-8458. http://www.minsocam.org/

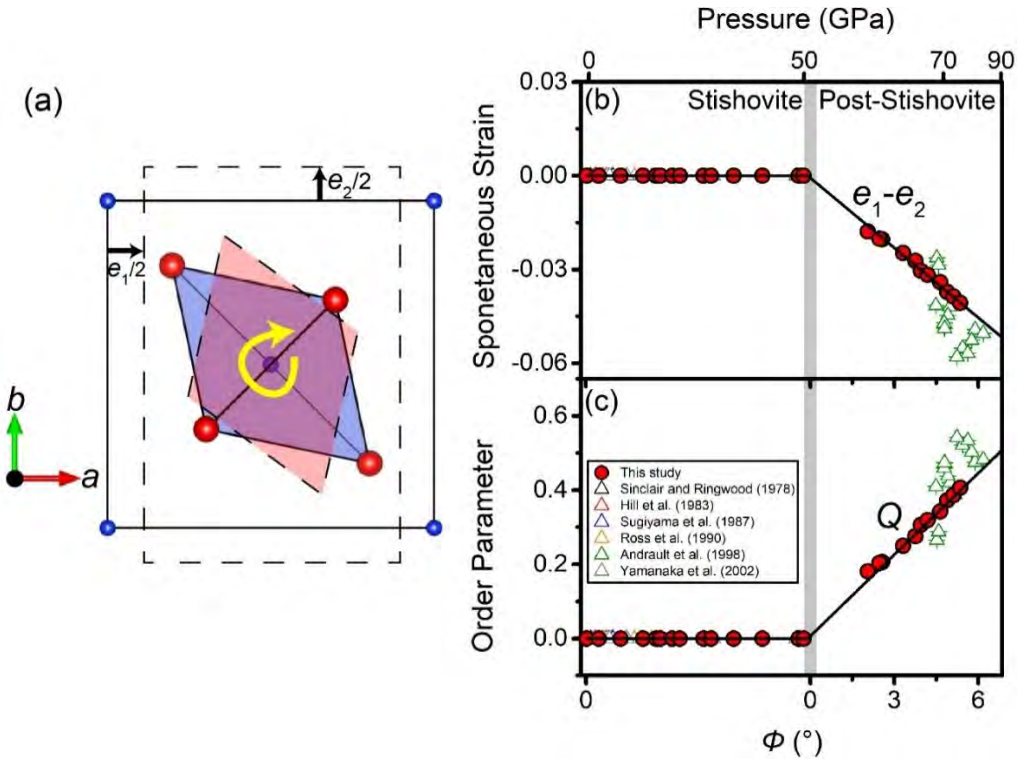

Fig 7